Nano Research 2015, 8(2): 666–672
DOI 10.1007/s12274-014-0550-8
Research Article
ISSN 1998-0124
CN 11-5974/O4

Thermoelectric transport across graphene/hexagonal boron nitride/graphene heterostructures

Chun-Chung Chen[1], Zhen Li[1], Li Shi[2], and Stephen B. Cronin[1] (✉)

[1] *Department of Electrical Engineering, University of Southern California, Los Angeles, CA 90089, USA*
[2] *Department of Mechanical Engineering and Texas Materials Institute, University of Texas at Austin, Texas 78712, USA*

Received: 27 May 2014
Revised: 8 July 2014
Accepted: 28 July2014

KEYWORDS
graphene,
boron nitride,
2D materials,
heterostructure,
thermoelectric

ABSTRACT

We report thermoelectric transport measurements across a graphene/hexagonal boron nitride (*h*-BN)/graphene heterostructure device. Using an AC lock-in technique, we are able to separate the thermoelectric contribution to the *I*–*V* characteristics of these important device structures. The temperature gradient is measured optically using Raman spectroscopy, which enables us to explore thermoelectric transport produced at material interfaces, across length scales of just 1–2 nm. Based on the observed thermoelectric voltage (ΔV) and temperature gradient (ΔT), a Seebeck coefficient of –99.3 μV/K is ascertained for the heterostructure device. The obtained Seebeck coefficient can be useful for understanding the thermoelectric component in the cross-plane *I*–*V* behaviors of emerging 2D heterostructure devices. These results provide an approach to probing thermoelectric energy conversion in two-dimensional layered heterostructures.

Electron transport in the cross-plane direction of layered material heterostructures has recently shown interesting new functionalities that extend far beyond lateral graphene devices. Graphene-based heterojunction devices, such as graphene/silicon and graphene/gallium arsenide diodes, have demonstrated rectifying behavior and gate-tunable photovoltaic responses [1–10] heterostructure devices made by combining graphene with other 2D materials, such as graphene/hexagonal boron nitride (*h*-BN)/graphene and graphene/MoS_2, have shown interesting electron tunneling transport, negative differential conductance, and light absorption behaviors [11–15]. In addition to electron transport and light absorption in these graphene-based heterojunctions, heat dissipation in these types of devices is found to be dominated by vertical heat transfer [16, 17]. Despite the large in-plane thermal conductivity in graphene and *h*-BN, the cross-plane thermal conductance of single- and few-layer graphene and *h*-BN can be rather small because of the atomic scale thickness. Hence, heat dissipation from these 2D heterostructure devices are often limited by thermal transport across the graphene/*h*-BN junction. A recent measurement has shown that the interface

Address correspondence to scronin@usc.edu

thermal conductance between graphene and *h*-BN is lower than theoretical prediction, likely caused by interface defects and contaminations [18]. While the low interface thermal conductance and potentially suppressed in-plane thermal conductivity in nano-patterned 2D structures is not desirable for electronic devices, it has stimulated interest in utilizing 2D layered heterostructures for thermoelectric conversion. For example, Xie et al. have reported a theoretical study of in-plane ballistic thermoelectric properties in boron nitride nanoribbons [19], and Yang et al. have simulated the in-plane thermoelectric properties in hybrid graphene/boron nitride nanoribbons [20]. Although it remains a question whether 2D hetero-structures can be useful for thermoelectric devices, their thermoelectric properties can influence the electron transport and heat dissipation behaviors of emerging 2D heterostructure devices [21]. Currently, there have been few experimental studies of ther-moelectric effects in 2D heterostructures.

Here, we report a thermoelectric transport measure-ment across a graphene/*h*-BN/graphene heterostructure. The thermovoltage is measured between the top and bottom graphene layers using an AC lock-in technique at frequency 2ω, based on Joule heating created in the top graphene layer with an AC voltage at ω. The top graphene layer is electrically heated by applying an AC voltage at frequency ω, which generates a heating power/temperature oscillating at 2ω, since $P = V^2/R$. The temperature gradient (oscillating at 2ω) results in electron diffusion between the top graphene (hot side) and bottom graphene (cold side), and hence a thermovoltage can be measured across the device at frequency 2ω. Using an AC lock- in amplifier to detect the 2ω thermovoltage separates the thermoelectric voltage from the other signals and noise in the system, enabling thermovoltages as small as microvolts to be detected. The temperatures of the top and bottom graphene layers are determined by monitoring their 2D band Raman frequencies, revealing temperature drops (ΔT) as high as 39 K between the top and bottom graphene layers. Since the temperatures are measured optically using Raman spectroscopy, we are able to explore thermoelectric transport across length scales of just 1–2 nm. From the measured thermoelectric voltage (ΔV) and the acquired temperature drops (ΔT) between the top and bottom graphene layers, the Seebeck coefficient (S) of the heterostructure device is established.

Figures 1(a) and 1(b) show an optical image and schematic diagram illustrating the profile structure of the graphene/*h*-BN/graphene device and the experi-mental setup. Here, the monolayer graphene is grown by chemical vapor deposition (CVD) with CH_4 at 1,000 °C on a copper foil, which is then transferred to a Si/SiO_2 substrate, and patterned to form a 3 μm × 100 μm bottom graphene strip using electron beam lithography (EBL) and oxygen plasma etching [22]. Another EBL and metal evaporation step is then performed to deposit Ti/Au electrodes on the bottom graphene strip. Multilayer (~5 layers) *h*-boron nitride (*h*-BN) is exfoliated using the "Scotch tape" method and deposited on another substrate. The multilayer *h*-BN flake is then transferred onto the center of the

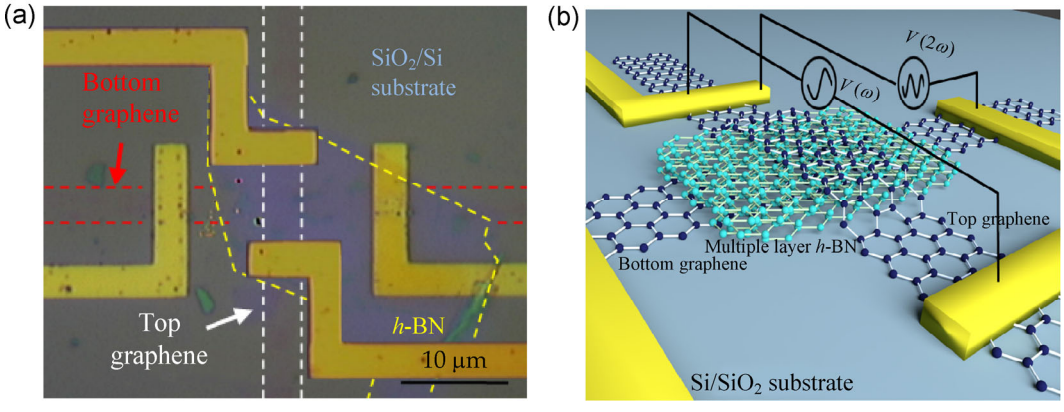

Figure 1 (a) Optical image and (b) schematic diagram of the graphene/*h*-BN/graphene/Al_2O_3 heterostructure device and measurement setup.

bottom graphene layer with careful alignment, using a sacrificial polymethylmethacrylate (PMMA) carried layer [23]. The top graphene strip is also fabricated by CVD growth on copper foil, transferred to another Si/SiO_2 substrate, EBL patterned and oxygen plasma etched, and then subsequently transferred with careful alignment to the bottom-graphene/*h*-BN overlapping region. During the last EBL and metal evaporation step, electrodes are deposited on the top graphene layer. Next, atomic layer deposition (ALD) is used to deposit a 60 nm insulating layer of Al_2O_3 on the surface of graphene/ *h*-BN/graphene heterostructure to make the device more robust. The fabricated device is then wire-bonded to a chip carrier for measurements carried out in vacuum.

Figure 2 shows the in-plane and cross-plane *I*–*V* characteristics of the bottom and top graphene strips. Unlike the in-plane *I*–*V* characteristics, the cross-plane transport shows a non-linear *I*–*V* curve, indicating electron tunneling through the graphene/*h*-BN/graphene heterojunction with a low-bias conductance (*G*) of 154 nS [11, 24] while the in-plane conductance are 20 and 23 μS, two orders of the magnitude higher than that of the cross-plane conductance. AC voltages with frequencies ω = 100 and 200 Hz are applied to the top graphene to provide a temperature drop between the graphene layers and induce a thermoelectric voltage across the graphene/BN/graphene heterostructure at the second harmonic frequencies, 200 and 400 Hz. The 2ω component of the thermoelectric voltage is a result of the 2ω component in the Joule heating in the top graphene layer. The applied AC voltages are kept below 2 V to protect the device and avoid unwanted substrate-induced doping and compression effects in the grapheme [25, 26]. In Fig. 3, the measured second harmonic thermoelectric voltage is plotted as a function of the applied AC voltage for both 100 and 200 Hz. Both datasets show the measured thermoelectric voltage increasing quadratically with the applied AC voltage, reaching 4 mV at 2 V of the applied voltage.

In order to determine the temperature of the graphene layers, the Raman spectra of the graphene layers are measured as a function of the applied voltage. However, independent measurement of temperature of two graphene layers at the region of the heterojunction

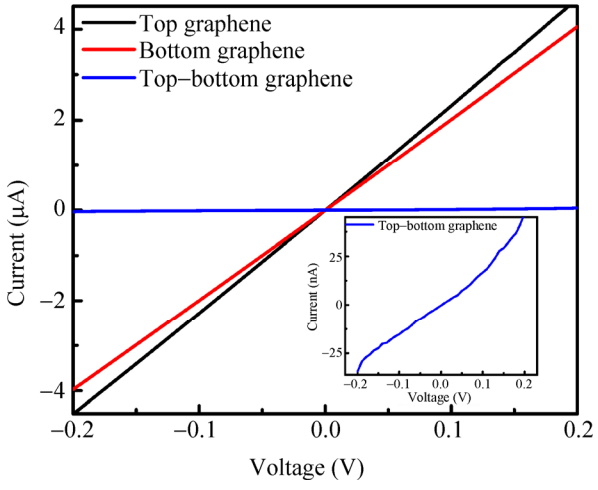

Figure 2 In-plane and cross-plane *I*–*V* characteristics of the bottom and top graphene strips of the heterostructure, the inset figure plots the cross-plane *I*–*V* characteristics with the units of nA.

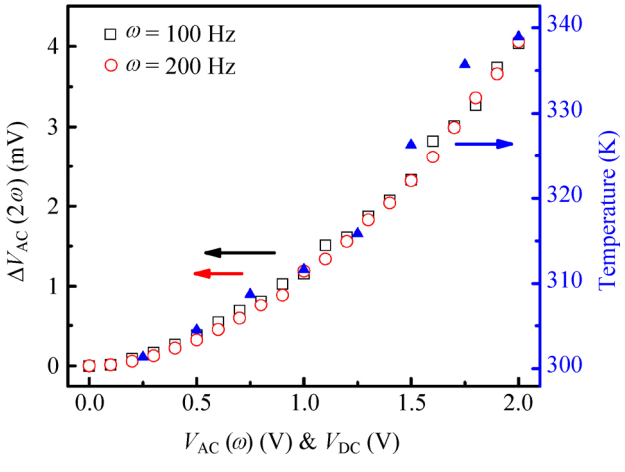

Figure 3 The 200 and 400 Hz thermoelectric voltages across the graphene/BN/graphene heterostructure as a function of the applied 100 and 200 Hz AC voltages together with the corresponding DC voltages measured at top graphene temperature (right axis).

where the two graphene layers overlap is not possible, since the acquired Raman signal from the top and bottom graphene layers cannot be distinguished. The temperatures of the two graphene layers can only be observed next to the heterojunction, between the junction and the electrodes, as indicated as points 1, 2, and 3 in Fig. 4(a). The 2D band Raman frequencies taken from the top graphene layer at point 1 and 2 downshift linearly with the increasing applied voltage, indicating Joule heating in the top graphene layer, while no frequency shift is observed in the bottom layer at point 3, as shown in Figs. S1(b), S1(c), and S1(d)

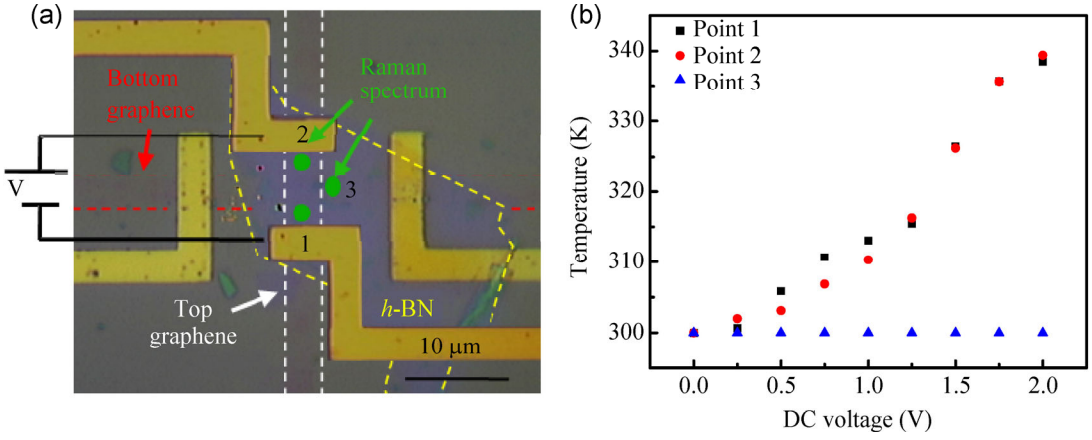

Figure 4 (a) Optical image indicating the locations of Raman spectra taken near the heterojunction. (b) Temperature of the graphene at the indicated location with respect to the applied voltage.

in the Electronic Supplementary Material (ESM). The temperature coefficients of the Raman frequencies for the top graphene layer are then calibrated in a temperature controlled stage and plotted in Figs. S2(a) and S2(b) (in the ESM), giving coefficients of –0.029 and –0.035 cm^{-1}/K at point 1 and point 2, respectively.

Here, the thermoelectric voltage is measured with AC Joule heating applied to the top graphene layer, while the temperature of the top graphene layer is calibrated as a function of DC heating. In order to ensure that an accurate comparison can be made between AC and DC heating, we calculate that the thermal time constant of the measured device is faster than the heating frequency. Because the thermal conductivity of the Si substrate is much larger than the 300 nm thick SiO_2 layer, heating is assumed to occur only in and above the SiO_2 layer. As such, the thermal time constant is controlled by the thermal resistance (R) and thermal capacitance (C) of the SiO_2 layer under the 3 μm × 3 μm heated graphene region. The thermal resistance of the SiO_2 layer is, thus, calculated to be on the order of 25,000 K/W. For the thermal capacitance, we conservatively assume that the heated region extends in the lateral direction five times beyond that of the heterostructure, which gives an area of 15 μm× 15 μm and a thermal capacitance of 1.8×10^{-10} J/K. Thus, the thermal time constant is obtained as $\tau = RC = 4.5$ μs, which corresponds to a cutoff frequency of 36 kHz. This value is more than two orders of magnitude higher than the AC frequencies applied here, so that the AC thermal impedance of the system can be reduced to the DC case, namely the ratio between the AC temperature rise and AC heating power is very close to that between the DC temperature rise and DC heating power [27, 28]. This conclusion is further supported by our measurement results conducted with heat frequencies of 100 and 200 Hz, which yield approximately the same results.

By converting the Raman downshifts to the AC component of the temperature rise, using the acquired temperature coefficients from the DC calibration, the temperature of the top graphene can be obtained, as plotted in Fig. 4(b), showing the temperature rise due to the Joule heating at points 1 and 2. Since no shift in the Raman frequency of the bottom graphene layer is observed, we obtain an upper limit for the temperature drop, and hence a lower limit of the Seebeck coefficient ($S = \Delta V/\Delta T$). Our ΔT measurement is limited to an upper bound because lateral temperature gradients may exist, and thus, the actual temperature drop directly across the heterostructure may be less than the measured ΔT. In this case, the Seebeck coefficient would be larger than that measured here. Assuming no lateral temperature gradients, we plot the measured thermoelectric voltage (ΔV) as a function of the cross-plane temperature gradient (ΔT) in Fig. 5 for the 100 and 200 Hz datasets. Here, a consistent linear dependence is observed between the voltage and the temperature gradient, yielding Seebeck coefficients of –97.1 μV/K and –99.3 μV/K for the 100 and 200 Hz datasets, respectively, which are higher than the in-

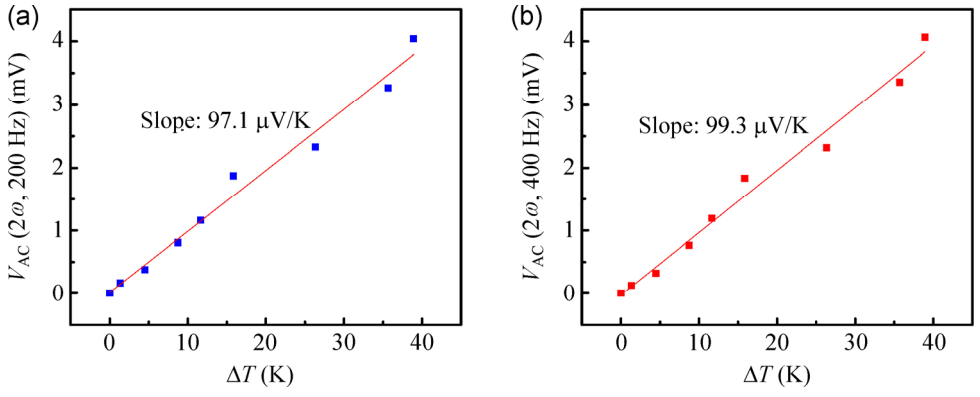

Figure 5 (a) The 200, and (b) 400 Hz thermoelectric voltage as a function of the maximum possible temperature drop (ΔT) across the heterostructure.

plane Seebeck coefficients of single layer graphene, ~50 μW/K, at room temperature [29]. The Seebeck coefficient is negative in these devices, since the band offsets (and hence energy barriers) between graphene and BN are much smaller for electrons than holes. From these observations, we estimate the power factor (S^2G) to be 1.46 and 1.51 × 10^{-15} W/K^2 for the graphene/*h*-BN/graphene heterojunctions. These power factors are extremely small because of the low electrical conductance of the BN. Here, we deliberately made the BN layer thick enough to suppress quantum mechanical tunneling. While it is possible that the cross-plane Seebeck coefficient consists of contributions from both electron tunneling [30, 31] and thermionic emission across the energy barrier [32, 33], further work is needed to determine what the dominant contribution is. The temperature drop is plotted as a function of the applied electrical power in Fig. S3 (in the ESM). Based on these data, we can calculate the thermal conductance (K) of the graphene/BN/graphene heterostructure using the equation "$K = Q/\Delta T$", where Q is the applied electrical heating power and ΔT is the temperature gradient across the heterostructure, which yields the thermal conductance of 4.25 × 10^{-7} W/K [18, 23]. Our measurement technique is not able to separate the electron and phonon contributions to the thermal conductance. However, we expect the phonon contribution to dominate in this system, since the electron density is rather low. We further obtain [19, 34] the thermoelectric figure of merit of this device as $ZT = S^2GT/K$, where T = 300 K is the temperature of the device and K is the thermal conductance across the heterostructure, yielding a ZT value of 1.05 × 10^{-6}. The low value of ZT observed here is most likely due to the large energy barrier across the graphene/*h*-BN interface (~0.5 eV). For efficient thermionic emission, barriers closer to k_BT should be utilized. We believe further enhancement in ZT can be achieved by optimizing the energy barrier height and the thickness of the *h*-BN flakes. It may be possible to vary the energy barrier at the graphene/BN interface by either doping or applying a DC bias voltage. However, application of a bias voltage will also lead to a substantial transfer of electrons across the interface due to tunneling through the barrier and thermionic emission over the energy barrier, and therefore thicker BN flakes would be required to avoid or understand the role of this tunneling current. A more systematic study as a function of BN thickness and bias voltage would have to be carried out in order to provide a complete understanding of this phenomenon. Here, we present a basic thermoelectric measurement across this interface in its simplest configuration.

In conclusion, we report Seebeck measurements across a graphene/*h*-BN/graphene heterostructure by inducing a temperature gradient between the bottom and top graphene layers and measuring the corresponding thermoelectric voltage (ΔV) across the heterostructure. A temperature gradient (ΔT) of 39 K and thermoelectric voltage (ΔV) of almost 4 mV is observed in the device, which results in a Seebeck coefficient of –99.3 μV/K, a power factor (S^2G) of 1.51 × 10^{-15} W/K^2, and a thermoelectric figure of merit

of $ZT = 1.05 \times 10^{-6}$ for the graphene/*h*-BN/graphene heterostructure. These measurements represent thermoelectric voltages produced at material interfaces, across length scales of just 1–2 nm. While the overall thermoelectric energy conversion efficiency of this device is small, the relatively large Seebeck coefficient and temperature drops observed here indicate that the *I*–*V* characteristics of 2D heterostructures can contain an appreciable thermoelectric component. The performance of graphene/BN/graphene heterostructure devices (i.e., tunneling transistors and diodes) will, therefore, be influenced by such thermoelectric effects.

Acknowledgements

This research was supported by DOE Award Nos. DE-FG02-07ER46376 and DE-FG02-07ER46377.

Electronic Supplementary Material: Supplementary material is available in the online version of this article at http://dx.doi.org/10.1007/s12274-014-0550-8.

References

[1] Chen, C.C.; Aykol, M.; Chang, C. C.; Levi, A. F. J.; Cronin, S. B. Graphene-silicon Schottky diodes. *Nano Lett.* **2011**, *11*, 1863–1867.

[2] Chen, C.C.; Chang, C. C.; Li, Z.; Levi A. F. J.; Cronin, S. B. Gate tunable graphene-silicon Ohmic/Schottky contacts. *Appl. Phys. Lett.* **2012**, *101*, 223113.

[3] Cui, T.X.; Lv, R. T.; Huang, Z. H.; Chen, S. X.; Zhang, Z. X.; Gan, X.; Jia, Y.; Li, X. M.; Wang, K. L.; Wu, D. H.; Kang, F. Y. Enhanced efficiency of graphene/silicon heterojunction solar cells by molecular doping. *J. Mater. Chem. A* **2013**, *1*, 5736–5740.

[4] Jie, W.; Zheng, F.; Hao, J. Graphene/gallium arsenide-based Schottky junction solar cells. *Appl. Phys. Lett* **2013**, *103*, 233111.

[5] An, X. H.; Liu, F. Z.; Kar, S. Optimizing performance parameters of graphene-silicon and thin transparent graphite-silicon heterojunction solar cells. *Carbon* **2013**, *57*, 329–337.

[6] Shi, E. Z.; Li, H. B.; Yang, L.; Zhang, L. H.; Li, Z.; Li, P. X.; Shang, Y. Y.; Wu, S. T.; Li, X. M.; Wei, J. Q.; Wang, K. L.; Zhu, H. W.; Wu, D. H.; Fang, Y.; Cao, A. Y. Colloidal antireflection coating improves graphene-silicon solar cells. *Nano Lett*. **2013**, *13*, 1776–1781.

[7] Li, X.; Fan, L. L.; Li, Z.; Wang, K. L.; Zhong, M. L.; Wei, J. Q.; Wu, D. H.; Zhu, H. W. Boron doping of graphene for graphene-silicon p–n junction solar cells. *Adv. Ener. Mater.* **2012**, *2*, 425–429.

[8] Lin, Y. X.; Xie, D.; Chen, Y.; Feng, T. T.; Shao, Q. M.; Tian, H.; Ren, T. L.; Li, X. M.; Li, X.; Fan, L. L.; Wang, K. L.; Wu, D. H.; Zhu, H. W. Optimization of graphene/silicon heterojunction solar cells. In *Preceedings of 2012 38th IEEE Photovoltaic Specialists Conference (Pvsc)*, **2012**. 2566–2570.

[9] Feng, T. T.; Xie, D.; Lin, Y. X.; Zhao, H. M.; Chen, Y.; Tian, H.; Ren, T. L.; Li, X.; Li, Z.; Wang, K. L.; Wu, D. H.; Zhu, H. W. Efficiency enhancement of graphene/silicon-pillar-array solar cells by HNO_3 and PEDOT-PSS. *Nanoscale* **2012**, *4*, 2130–2133.

[10] Won, R. Photovoltaics: Graphene-silicon solar cells. *Nat. Photonics* **2010**, *4*, 411.

[11] Britnell, L.; Gorbachev, R. V.; Jalil, R.; Belle, B. D.; Schedin, F.; Katsnelson, M. I.; Eaves, L.; Morozov, S. V.; Mayorov, A. S.; Peres, N. M. R.; Neto, A. H. C.; Leist, J.; Geim, A. K.; Ponomarenko, L. A.; Novoselov, K. S. Electron tunneling through ultrathin boron nitride crystalline barriers. *Nano Lett.* **2012**, *12*, 1707–1710.

[12] Britnell, L.; Gorbachev, R. V.; Jalil, R.; Belle, B. D.; Schedin, F.; Mishchenko, A.; Georgiou, T.; Katsnelson, M. I.; Eaves, L.; Morozov, S. V.; Peres, N. M. R.; Leist, J.; Geim, A. K.; Novoselov, K. S.; Ponomarenko, L. A. Field-effect tunneling transistor based on vertical graphene heterostructures. *Science* **2012**, *335*, 947–950.

[13] Britnell, L.; Gorbachev, R. V.; Geim, A. K.; Ponomarenko, L. A.; Mishchenko, A.; Greenaway, M. T.; Fromhold, T. M.; Novoselov, K. S.; Eaves, L. Resonant tunnelling and negative differential conductance in graphene transistors. *Nat. Comm.* **2013**, *4*, 1794.

[14] Kim, S.; Shin, D. H.; Kim, C. O.; Kang, S. S.; Kim, J. M.; Jang, C. W.; Loo, S. S.; Lee, J. S.; Kim, J. H.; Choi, S. H.; Hwang, E. Graphene p–n vertical tunneling diodes. *ACS Nano* **2013**, *7*, 5168–5174.

[15] Roy, K.; Padmanabhan, M.; Goswami, S.; Sai, T. P.; Ramalingam, G.; Raghavan, S.; Ghosh, A. Graphene-MoS_2 hybrid structures for multifunctional photoresponsive memory devices. *Nat. Nanotechnol.* **2013**, *8*, 826–830.

[16] Jo, I.; Hsu, I. K. Lee, Y. J.; Sadeghi, M. M.; Kim, S.; Cronin, S.; Tutuc, E.; Banerjee, S. K.; Yao, Z.; Shi, L. Low-Frequency acoustic phonon temperature distribution in electrically biased graphene. *Nano Lett.* **2011**, *11,* 85–90.

[17] Pop, E.; Varshney, V.; Roy, A. K. Thermal properties of graphene: Fundamentals and applications. *Mrs Bulletin* **2012**, *37*, 1273–1281.

[18] Chen, C. C.; Li, Z.; Shi, L.; Cronin, S. B. Thermal interface conductance across a graphene/hexagonal boron nitride heterojunction. *Appl. Phys. Lett.* **2014**, *104*, 081908.

[19] Xie, Z. X.; Tang, L. M.; Pan, C. N.; Chen, Q.; Chen, K. Q. Ballistic thermoelectric properties in boron nitride nanoribbons. *J. Appl. Phys.* **2013**, *114*, 144311.

[20] Yang, K. K.; Chen, Y. P.; D'Agosta, R.; Xie, Y. E.; Zhong, J. X.; Rubio, A. Enhanced thermoelectric properties in hybrid graphene/boron nitride nanoribbons. *Phys. Rev. B* **2012**, *86*, 045425.

[21] Grosse, K. L.; Bae, M. H.; Lian, F. F.; Pop, E.; King, W. P. Nanoscale Joule heating, Peltier cooling and current crowding at graphene-metal contacts. *Nat. Nanotechnol.* **2011**, *6*, 287–290.

[22] Li, X. S.; Cai, W. W.; An, J. H. Kim, S.; Nah, J.; Yang, D. X.; Piner, R.;Velamakanni, A.; Jung, I.; Tutuc, E.; Banerjee, S. K.; Colombo, L.; Ruoff, R. S. Large-area synthesis of high-quality and uniform graphene films on copper foils. *Science* **2009**, *324*, 1312–1314.

[23] Jo, I.; Pettes, M. T.; Kim, J.; Watanabe, K.; Taniguchi, T.; Yao, Z.; Shi, L. Thermal conductivity and phonon transport in suspended few-layer hexagonal boron nitride. *Nano Lett.* **2013**, *13*, 550–554.

[24] Lee, G. H.; Yu, Y. J.; Lee, C.; Dean, C.; Shepard, K. L.; Kim, P.; Hone, J. Electron tunneling through atomically flat and ultrathin hexagonal boron nitride. *Appl. Phys. Lett.* **2011**, *99*, 243114.

[25] Chen, C. C.; Bao, W. Z.; Theiss, J.; Dames, C.; Lau, C. N.; Cronin, S. B. Raman spectroscopy of ripple formation in suspended graphene. *Nano Lett.* **2009**, *9*, 4172–4176.

[26] Chen, C. C.; Bao, W. Z.; Chang, C. C.; Zhao, Z.; Lau, C. N.; Cronin, S. B. Raman spectroscopy of substrate-induced compression and substrate doping in thermally cycled graphene. *Phys. Rev.* B, **2012**, *85*, 035431.

[27] Shi, L.; Li, D. Y.; Yu, C. H.; Jang, W. Y.; Kim, D. Y.; Yao, Z.; Kim, P.; Majumdar, A. Measuring thermal and thermoelectric properties of one-dimensional nanostructures using a microfabricated device. *J. Heat Trans. T. Asme* **2013**, *125*, 1209–1209.

[28] Yamane, T.; Nagai, N.; Katayama, S.; Todoki, M. Measurement of thermal conductivity of silicon dioxide thin films using a 3 omega method. *J. Appl. Phys.* **2002**, *91*, 9772–9776.

[29] Li, X. M.; Yin, J.; Zhou, J. X.; Wang, Q.; Guo, W. L. Exceptional high Seebeck coefficient and gas-flow-induced voltage in multilayer graphene. *Appl. Phys. Lett.* **2012**, *100*, 183108.

[30] Cho, S.; Kang, S. D.; Kim, W.; Lee, E. S.; Woo, S. J.; Kong, K. J.; Kim, I.; Kim, H. D.; Zhang, T.; Stroscio, J. A.; Kim, Y. H.; Lyeo, H. K. Thermoelectric imaging of structural disorder in epitaxial graphene. *Nat. Mater.* **2013**, *12*, 913–918.

[31] Lee, E. S.; Cho, S.; Lyeo. H. K.; Kim, Y. H. Seebeck effect at the atomic scale. *Phys. Rev. Lett*. **2014**, *112*, 136601.

[32] Mahan, G. D.; Woods, L. M. Multilayer thermionic refrigeration. *Phys. Rev. Lett*. **1998**, *80*, 4016–4019.

[33] Mahan, G. D.; Sofo, J. O.; Bartkowiak, M. Multilayer thermionic refrigerator and generator. *J. Appl. Phys.* **1998**, *83,* 4683–4689 .

[34] Majumdar, A. Thermoelectricity in semiconductor nanostructures. *Science* **2004**, *303*, 777–778.